Competition between the Photothermal Effect and Emission in Potential Phototherapy Agents

Valentin Diez-Cabanes, Antonio Monari, Mariachiara Pastore

The Competition between Photothermal Effect and Emission in Potential Phototherapy Agents

Valentin Diez-Cabanes,[1,*] *Antonio Monari,*[1] *Mariachiara Pastore*[1,*]

[1] Université de Lorraine & CNRS, Laboratoire de Physique et Chimie Théoriques (LPCT), UMR 7019, F-54000, Nancy, France

*Authors to whom correspondence should be addressed: valentin.diez-cabanes@univ-lorraine.fr; mariachiara.pastore@univ-lorraine.fr

KEYWORDS Photothermal Therapy, Small Organic Molecules, Charge Transfer, Density Functional Theory, Molecular Dynamics

ABSTRACT

Planar donor-acceptor-donor (D-A-D) organic molecules have been highlighted as promising photothermal agents due to their good light-to-heat conversion ratio, easy degradation and chemical tunability. Very recently, it has been demonstrated that their photothermal conversion can be boosted by appending rather long alkyl chains. Despite this behavior has been tentatively associated to the population of a non-radiative twisted intramolecular charge transfer (TICT) state driven by intramolecular motion, the precise mechanisms and the role played by the environment, and most notably aggregation, still remain elusive. In this context, we carried a series of Time-Dependent Density Functional Theory (TD-DFT) calculations combined with Molecular Dynamics (MD) simulations to achieve a realistic description of the isolated and aggregated

systems. Our theoretical models unambiguously evidence that the population of CT states is very unlikely in both cases, whereas the light- triggered heat dissipation can be ascribed to the activation of specific vibrational degrees of freedom related to the relative motion of the peripheral chains. Overall, our results clearly corroborate the active role played by the alkyl substituents in the photothermal conversion through vibrational motion, while breaking with the conventional picture, which invokes the formation of dark TICT states in non-close packed aggregates.

Introduction

Heterogenous light-triggered activated photothermal therapy (PTT) agents present several advantages with respect to other anticancer clinical treatments (i.e. radio- or chemo-therapy) due to their high selectivity and sensitivity, and low invasiveness, which results in a strongly reduced damages to the surrounding health tissues and hence a strong decrease of unwanted side-effects limiting the patients' quality of life.[1–5] PTT is based in the exploitation of a dye that after absorption of a suitable light wavelength will thermally relax producing a localized increase of the temperature that is susceptible to disrupt the cellular organization leading to the triggering of apoptotic pathways or its necrosis. To date, most of the materials used for PTT are based on inorganic or metallic nanoparticles. Despite showing some important advantages such as large absorption coefficients, good photostability and excellent performance, their practical use is however limited by their toxicity and scarce biodegradability leading to accumulation in the tissues.[6–8] To overcome this issue, organic PTT agents in form of small molecules[9–11] or polymers[12–14] have been recently proposed as promising light-activated agents due to their low cost, easy decomposition, and high versatility. Indeed, their optical properties can be opportunely tuned via

chemical engineering.[15–18] The most common organic molecules used in clinical applications are based on cyanine-based agents, being indocyanine green (ICG) the workhorse component employed in these fields.[19,20] By the way, their practical application has been limited due to their poor stability in biological environments, low target selectivity, and quick released from human body.[21] In view of their higher photostability and good biocompatibility, a great attention has been devoted, during the last years, to small planar acceptor (A) molecules such as diketopyrrolopyrroles,[22] naphthalene diimides,[23] thiadiazoles,[24,25] or fluorenes.[26] Remarkably, the extended π-conjugation of their cores combined with donor groups conforming a D-A-D architecture, allows these materials to display large absorption coefficients in the NIR region, hence reaching the therapeutic wavelength limit, and efficient quantum yields in solution.

Following NIR activation, the specific biological application will depend on the relaxation pathways of the photogenerated electronical excited state. If the populated excited state is emissive the organic agents can be used as fluorescence or luminescent dyes and hence be used as probes for bioimaging applications. Whereas if their excited state thermally dissipates through non-radiative relaxation, they can be used for PTT. In this context, the deep understanding of the photophysics driving the relaxation processes of the generated states is crucial if one wants to optimize the PTT conversion by proper structural modifications.[27] Nevertheless, the knowledge of the intrinsic photophysical properties of the organic molecules alone is usually not sufficient, since in biological applications the dyes are embedded in a complex and inhomogeneous environment or are subjected to aggregation. Indeed, contrary to inorganic semiconductors, small organic molecules are highly polarizable,[28] meaning that their optical response is quite sensitive to their surroundings.[29] On the same foot, in case of the formation of stable aggregates, the electronic excited states centered on the different units may start to couple, resulting in a completely different

optical and photophysical behavior with respect to the single molecule, due to the formation of delocalized excitonic states.[30] This phenomenon is especially relevant when the molecular aromatic cores are forming π-stacked aggregates, which can also trigger different physical processes such as inter- or intra-molecular charge transfer.[31] In this case one can observe the quenching of luminescence through the so-called aggregation caused quenching (ACQ).[32] Nonetheless, molecular stacking is not necessarily related to quenching. Indeed, the luminescence of certain molecules whose excited states can deactivate non-radiatively through large scale molecular vibrations, such as rotation of peripheral groups, can be substantially enhanced by blocking these deactivation channels in the solid state or in the close packed aggregates.[33] This phenomenon is commonly known as aggregation induced emission (AIE)[32,34,35] and it has been recently reported for some organic fluorophores such as diketopyrrolopyrrole-based and sulfonamide dyes. Overall, we can conclude that chemical substituents which enable/disable the intermolecular motion at the solid (aggregate) state are crucial in mediating the photophysical outcome of the material.[15,36]

In this viewpoint, one interesting strategy which allows to control the molecular packing of dyes is the functionalization with saturated alkyl chains. The resulting photophysics being strongly dependent on the characteristics (length, substitution position, etc.) of the peripheral chains. One paradigmatic example of this phenomenon has been recently reported,[25] where the photothermal performance of a given NIR-II dyes was finely adjusted by employing four different alkyl chains of increasing length. These dyes consist of a planar D-π-A-π-D core, where a benzo[1,2-c:4,5-c′]bis([1,2,5]thiadiazole) (BBTD) moiety, acting as acceptor, is connected to two terminal triphenylamine (TPA) donor groups by means of two π-conjugated thiophene bridges (see Figure 1). The saturated chains are inserted in ortho- position with respect to the TPA groups, and their

length ranges from a short 1-hexyl chain (**1**) to a long 2-decylmyristyl group (**2**). Interestingly, both dyes exhibited a broad emission in solution which was significantly quenched when moving to aggregates, i.e incorporating them in mixed-shell nanoparticles. More importantly, the photothermal efficiency of the NP aggregates was considerably enhanced when increasing the length of the saturated chains, resulting in a photothermal conversion capacity outperforming the commercial green ICG. This behavior was attributed by the authors to the population of a dark twisted intramolecular charge transfer (TICT) state, that should be favored in case of the longer alkyl spacer thanks to a less compact packing and hence to a higher flexibility in the aggregate state. These findings opened the door to the use of photo induced intramolecular motions for phototherapy purposes.[24] In a following up work, the same authors investigated the emission mechanisms of the same dyes, but this time the hexyl chains were linked to the TPA unit via a meta- connection. In this case, the shielding effect of the peripheral chains in the aggregates was supposed to block the intramolecular motion, inhibiting the population of the TICT state, and hence resulting in a AIE.[37] Furthermore, the same authors indicated that the increase in the chain lengths leads to an intensification of AIE, which was ascribed to the prevention of undesired intermolecular interactions, which could originate ACQ processes.[38] In this context, the influence of the chain geometries in the stabilization of the TICT states, which are claimed to be the cause of the different behavior of these dyes in solution vs aggregated state, remains unclear. If the less-hindered intramolecular motion in the loosely packed aggregates (longer chains) was at the origin of the fluorescence quenching, the molecule in solution should also be not emissive, and this is not the case. As we can see, some of the explanations given in the literature to rationalize the emission properties of these dyes appear contradictory, while their elucidation will be crucial for the development of efficient imaging and PTT technologies based on small organic molecules.

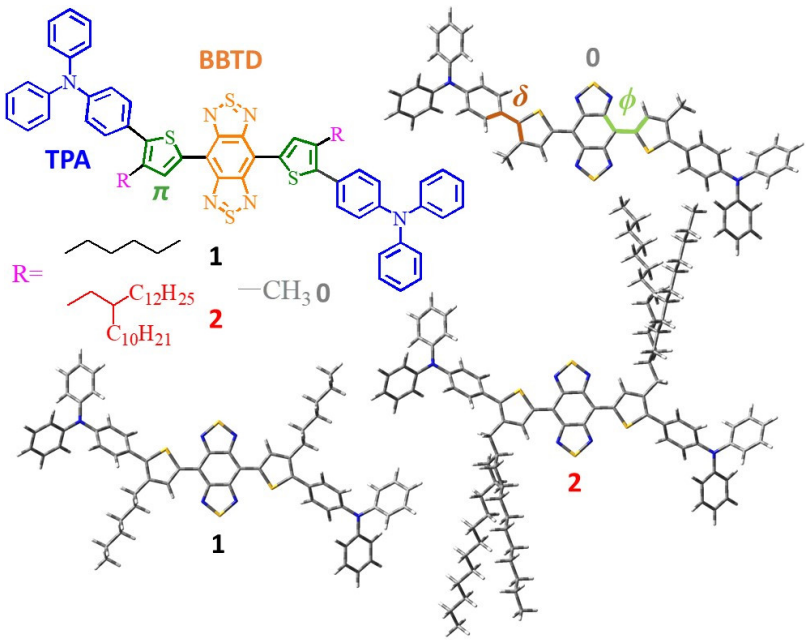

Figure 1. Chemical structure (top left) and ground state (GS) geometries (bottom) for **0**, **1** and **2** dyes.

Notably, molecular modelling and simulation has proven invaluable to shed light on the different physical phenomena underlying the optical and photophysical properties of organic dyes and the role played by the environment. This requires the combination of highly accurate methods to describe the excited states of the organic dye, with adequate computational strategies to treat the different environments in realistic conditions as well as the effects of the dynamical movement and the conformational sampling. Hence, to understand the basis of the PTT efficiency of the two aforementioned dyes we resorted to a multiscale simulation protocol in which Time-Dependent Density Functional Theory (TD-DFT) is used to get access to the excited states properties,[39,40] whereas for classical Molecular Dynamics (MD) is used to sample the phase space of large aggregates (>2000 atoms) up to hundreds of nanosecond timescale. As a matter of fact, this

strategy has been successfully applied to the study of the aggregation effects in other type of applications such as photovoltaic[41] or light emitting devices.[42]

In this work, we aim at understanding the influence of the chain length on the excited state relaxation pathways governing the emission mechanism of the prototype PTT agents displayed in Figure1, in solution and aggregates. Firstly, we investigated the possible population of TICT states by exploring the main characteristics of potential energy surface of the lowest lying excited states along some selected coordinates. In particular, we considered the coordinates describing the torsional intramolecular motion influencing the TICT energetic, namely the dihedral angles connecting the D-π-A groups (δ and ϕ angles in Figure 1). Afterwards, we evaluated the effect of the different environment (solution vs aggregation) for both short and long peripheral chain, by comparing the results obtained from monomers (solution) and dimer (representative of aggregates) MD trajectories. The most relevant degrees of freedom that can be connected to non-radiative deactivation channels are also evidenced by performing Principal Components Analysis (PCA) along the MD simulation. Globally, our theoretical results clearly show that the heat dissipation processes of the long-chain dyes originates from the activation of specific vibrational modes via the interaction of the bulky groups in the aggregated state, rather than by the population of TICT state. This emerging picture highlights the need for a chemical design aimed at favoring the interaction between bulky chains, instead of focusing on the intermolecular motions of the cores, if one wants to properly boost the photothermal conversion of planar D-A-D dyes. Before closing this section, it is noteworthy to mention that many different physical phenomena (vibronic coupling, dark (n,π*) or (σ,π*) states, etc.) could potentially influence the non-radiative pathways followed by the dye's excited states in their aggregated state.[43] Nonetheless, in view of the variety and complexity of these processes we intend to tackle them in prospective separated works.

Theoretical methods

Static Quantum Mechanics (QM) calculations

QM calculations were performed at the DFT level employing the CAM-B3LYP functional[44] and the 6-31G(d) basis set. This level of theory was chosen with the aim of properly describing CT states and the shape and energy barriers of the PES curves.[45–47] In static calculations, solvent (water) was treated by means of the Conductive Polarizable Continuum Model (C-PCM).[48] The excited state properties of the dyes were investigated by employing TD-DFT. A half-width at full-length of 0.17 eV was employed to build the static simulated TD-DFT spectra. The CT analysis was carried by analyzing the transition density matrices via the tools implemented in TheoDORE package.[49] On the same foot, Natural Transition Orbitals (NTOs) were used to obtain a spatial representation of the electronic density reorganization for the lowest energy states.[50] All QM calculations have been carried out within Gaussian16 package.[51]

MD simulations

For the FF parametrization and MD methodologies we relied on the procedure implemented in our previous work.[52] We employed a standard General Amber Force Field (GAFF),[53] where all parameters have been obtained with the antechamber program available in the AMBER16 package suite of tools. [54] Following the standard procedure established for AMBER, we assigned all atomic point-charges by computing the Restricted Electrostatic potential (RESP) charges estimated at the HF/6-31G* level of theory. In a last step, all FF parameters were converted into a suitable GROMACS file format by means of the ACPYPE - AnteChamber PYthon Parser interface program.[55]

All MM/MD simulations were conducted within GROMACS package suite of programs.[56] We first built an initial configuration for the MD simulations by immersing the **1** and **2** relaxed structures in a 50x50x50Å water solvent box by employing the Packmol package suite of tools.[57] The number of solvent molecules in the simulation box was chosen to match the density of water at room temperature: one **1**/**2** dye and 4120/4070 solvent molecules for the monomers **M1**/**M2**; and two **1**/**2** dyes and 4074/3975 water molecules in the case of the dimers **D1**/**D2**. For the sake of illustration, Figure S1 presents a perspective view of the four equilibrated solvent boxes considered here. The first equilibration run consisted of 100 ps simulation performed in the NVT ensemble, with a time step of 0.1 fs, where the geometries of the dyes were frozen to its equilibrium conformation. For this run, initial velocities were assigned by a random Maxwell-Boltzmann distribution at 298 K, whereas the temperature was controlled by a velocity rescaling thermostat.[58] Afterwards, a longer 10 ns NVT equilibration run was carried out by removing the previous constraints on the dyes, within the same set of parameters. In the last equilibration step, a 2.5 ns NPT run was performed at 298 K and 1 atm, with a 0.25 fs time-step, where the thermostated system was coupled to a Parrinello-Rahaman barostat.[59] Finally, the production run involved a 10 ns simulation, done in the NPT ensemble, at 1 atm and 298 K.

QM calculations for the MD snapshots

50 snapshots of the dye geometries along the MD run were used to calculate TD-DFT transition energies at the same level of theory as previously discussed. The thermalized averaged spectra were calculated by convoluting all vertical transitions with Gaussian function of half-width at full-length of 0.09 eV. The orientation factor $\varkappa$ which describes the relative position of the two monomers conforming the dimer configurations has been calculated as follows:

$$\kappa = \hat{\mu}_i \cdot \hat{\mu}_j - 3\left(\hat{\mu}_i \cdot \hat{R}\right)\left(\hat{\mu}_j \cdot \hat{R}\right) \quad (1)$$

Where $\mu_{i/j}$ represents the normalized transition dipole moment of the isolated monomers, and R is normalized vector connecting the centers of mass for both monomers.

Results and discussion

The static picture: Potential Energy Surface (PES)

We have started our investigation by analyzing the ground state (GS) structures of **1** and **2** displayed in Figure 1. Due to their conjugated nature, the two geometrical properties dictating the opto-electronic response are the twist dihedral angle connecting the TPA-π bridge units (δ), and the one between π-BBTD moieties (ϕ). The alkyl chains are in orto-(meta-) position with respect to the TPA(BBTD) groups, resulting in a larger influence of the chain geometry on the values of δ. Indeed, ϕ angles remain close to ideal planarity (2.3 and 2.5˚ for **1** and **2**), while δ angles are distorted due to the sizeable steric hindrance (47.1 and 43.6˚ for **1** and **2**). These values are in fair agreement with previous studies[25] and showed that both **1** and **2** exhibit comparable geometrical properties in their GS.

In a second step, we have investigated the possible population of TICT state by performing a series of TD-DFT calculations (see Experimental section), as this state has been invoked to explain the different emission patterns of **1** and **2**.[25] For the sake of simplicity, since the static optical properties of both dyes are only negligibly influenced by the length of their alkyl chains (see Table S1), we decided to employ a reduced model (**0**) where the peripheral chains are substituted by a methyl group (see Figure1), without strongly impacting the dye geometries (δ and ϕ amounted to 39.9˚ and 2.2˚ respectively in **0**). We have focused on the three lowest energy states of **0**, since the

other states are too high in energy (>3.4 eV) to be activated with NIR wavelengths. The nature of these states, at the Franck-Condon geometry, has been analysed by inspecting the corresponding Natural Transition Orbitals (NTOs),[50] which provides a spatial representation of the hole/electron couple, as exemplified in Figure 2. In addition, a quantitative estimation of the hole/electron localization along the different fragments has been obtained by performing the transition density matrix analysis implemented in the TheoDORE package[49] (see Table S2).

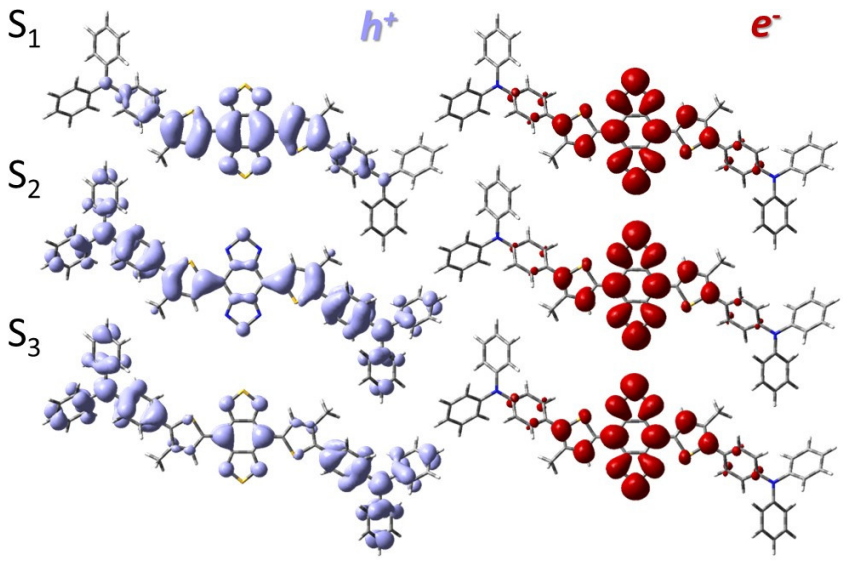

Figure 2. NTOs for S_1, S_2 and S_3 states in the GS geometry for the simplified dye **0**. The isovalue used to plot the isodensity was set to 0.02 a.u. Note that the NTOs for **1** and **2** are presented in Figure S2.

S_1 possess a local π-π* character localized around the BBTD moiety (87% / 96% of hole/electron localization on the π-BBTD-π fragment) with only a slight extension to the thiophene bridges. Thus, it presents a large oscillator strength in the NIR region, which clearly corresponds to the lowest absorption bands centred at 808 and 820 nm for **1** and **2** respectively, as measured experimentally.[25] On the other hand, S_2 and S_3 exhibit a prominent TPA to BBTD CT character

(68/77% and 80/77% of hole/electron localization along TPA/BBTD units for S_2 and S_3, respectively). This fact leads to much lower transition dipole moments and hence the states are almost dark (especially S_2). Note that an identical nature of the three lowest excited states was found in the full models for **1** and **2** (see Figure S2 and Table S2). More interestingly, our calculations pointed to a large energy difference (>1.1 eV) separating the bright S_1 and the dark CT S_2 and S_3 states at the optimal GS geometry (see Table 1). This finding already suggests that internal conversion leading to the population of the CT state should require surmounting a very important energetic penalty, that is most unlucky to be achieved through geometrical reorganization, even in presence of a twisted geometry. However, to verify this hypothesis we have explored the PES of the three lowest excited states. The energies at the equilibrium geometry of each of the states are reported in Table 1.

Table 1. Energies in eV of the three first excited states in the $S_{0\text{-}3}$ geometries of the simplified dye **0** with the corresponding oscillator strength in parenthesis for each excited state.

	excited state energy (eV)		
Geometry	S_1	S_2	S_3
S_0	1.38 (0.92)	2.49 (0.00)	2.82 (0.20)
S_1	0.86 (0.87)	2.15 (0.00)	2.57 (0.51)
S_2	1.03 (0.94)	2.12 (0.00)	2.59 (0.36)
S_3	1.11 (0.81)	2.24 (0.00)	2.54 (0.22)

The results provided in Table 1 unambiguously shows that the three states do not cross each other due to the high energy gap between them, being S_1 the lowest energy state for all cases. Furthermore, the GS geometries of the dyes were not largely modified upon relaxation of the

excited states (see Figure S3), hence similar twisting angles for all S_{0-3} geometries (see Table S4) have been observed. Note that these results are independent of the choice of the solvent (see Table S3). To get an even deeper exploration of the possible radiative channels that could involve larger structural deformations, we have obtained the PES of the three excited states along the δ and ϕ angles, as displayed in Figure 3.

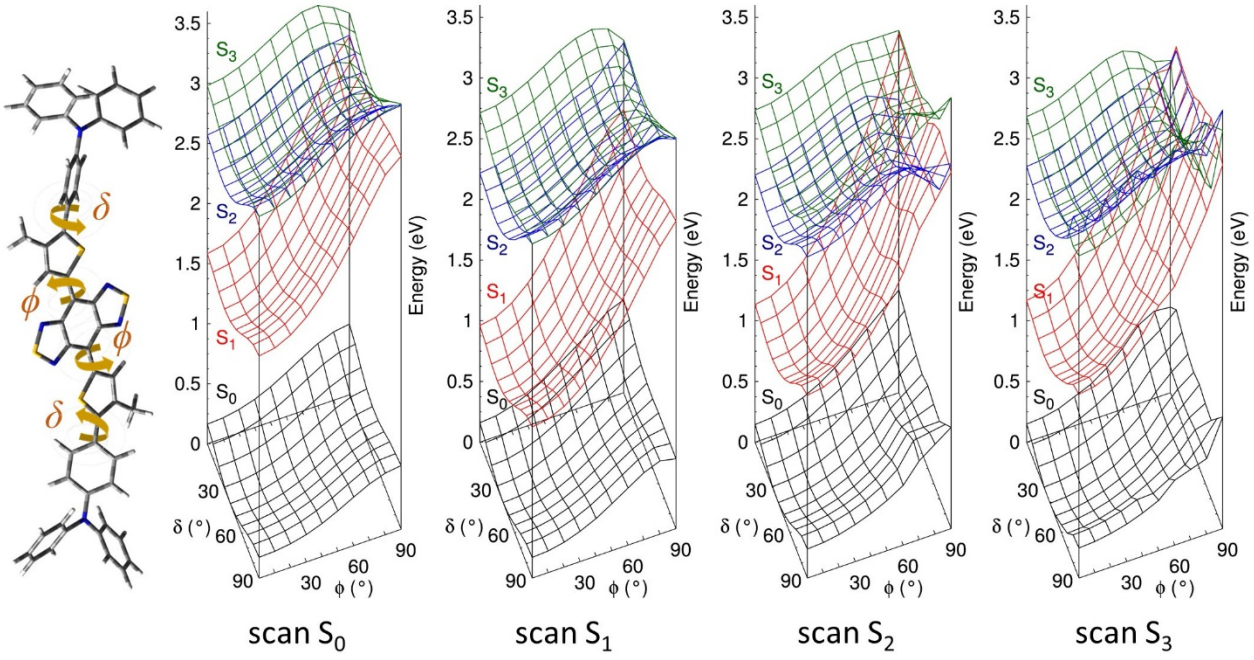

Figure 3. PES curves for the ground and three lowest excited states of **0**, estimated for δ and ϕ coordinates and obtained by relaxation of their S_0, S_1, S_2 and S_3 states. The δ and ϕ twist angles are illustrated on the right part of the curves and were kept rigid during the structural relaxation.

The four PES curves indicate that the energy gradients are mainly determined by values of ϕ rather than δ, which exhibited quite flat surfaces with an energy minimum around 45°. All states are destabilized when increasing ϕ from 0°, being this effect especially prominent in the case of S_1. This result is not surprising due to the break of the extended delocalization of this state over the thiophene units. However, following the relaxation on the S_0 and S_1 PES, the destabilization of

S_1 with respect to the higher energy states is not accompanied by any crossing between the excited states, even for ϕ values close to 90°. Nevertheless, in the case of S_2 and S_3 PES, we can hint at the presence of conical intersection (CI) between S_2 and S_3, and S_1 for ϕ angles equal to 75° and 85°, respectively. Despite having located CIs which could lead to TICT, those non-adiabatic points appear scarcely accessible since the barrier on the S_1 PES amount to 1.4 eV and 1.5 eV for S_2 and S_3 crossings, i.e. more than 50 times larger than kT at room temperature, and hence out of reach even considering an excess of kinetic energy due to excitation. These results unequivocally demonstrate the absence of TICT for these dyes in solution, as indicated by their measured emission spectra. We can thus proceed to evaluate the behaviour of the same compounds in an aggregated-state via MD simulations.

Dynamic response: self-aggregation and non-radiative recombination

To achieve a realistic description of the environmental effect affecting the dyes both in solution and in aggregates, we relied on the use of MD simulations, as described in the Theoretical Methods section and in the SI. More in detail, the behavior of the dyes in solution has been studied by considering only one molecule (monomer) in the simulation box (**M1** and **M2** for **1** and **2** dyes, respectively), whereas aggregation has been simulated by introducing a second dye in the box, thus resulting in a dimer configuration, **D1** and **D2** for **1** and **2**, respectively. Water has been chosen as solvent in view of its relevance in biological applications and the available experimental data.[25] Note that for an accurate representation of the molecular geometries along the dynamics one should consider the relaxation of the lowest energy state as well. Nevertheless, in view of both the huge computational burden required by this type of dynamics (especially for the timescales employed here ~10 ns), and the almost negligible geometrical changes obtained when relaxing the lowest

energy states from the dye GS geometries (see Figure S3), we consider that the GS geometries obtained by our model are suitable for the objectives tackled in this study.

In view of their close structure, one may expect a similar behavior of **1** and **2** dyes in solution, nevertheless this is not the case in the aggregated state, where the length of the chains can definitely modulate the interaction between the dye cores. Coherently, we focus our attention on the analysis of the geometrical factors describing the interaction between the monomers in **D1** and **D2** (Figure 4-a and 4-b). In particular, we have evaluated the evolution of two geometrical descriptors along the MD trajectory: the distance between the centers of mass and the tilting angle between the long axes of the two monomers' cores, as represented in Figure 4-b. The distribution of these two variables is presented in Figure 4-c. In the case of **D1**, the relatively short hexyl chains of the monomers do not hinder the aggregation between the dye molecules (see Figure 4-a left), resulting in a core distance peaking at 4Å and tilting angles centred around 22°, which are typical values for π-stacked aggregated structures.[60] On the other hand, the bulky and flexible chains of **D2** hampers the stacking between the monomer cores, leading to disordered dimer configurations with a broader distribution of both descriptors. More in detail, the inter-core distance peaks at 10.5Å and the tilting angle at 40°, thus suggesting a negligible tendency to form ordered aggregates for this dye.

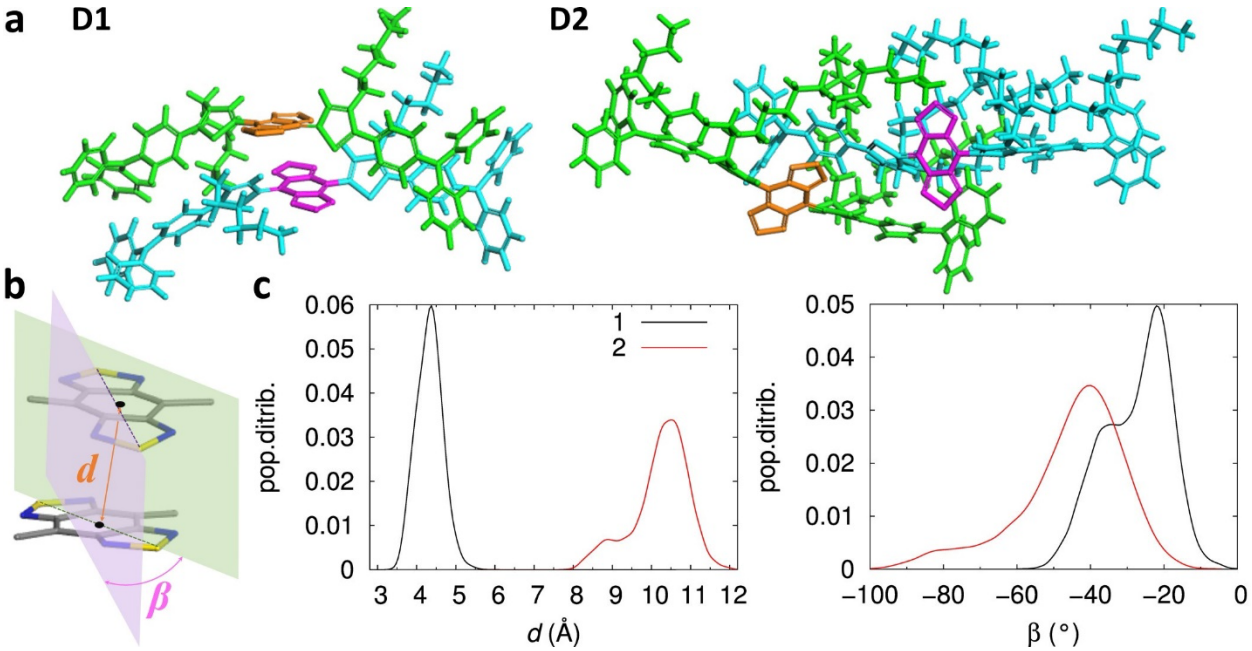

Figure 4. a) Perspective view of a representative snapshot for **D1** and **D2** geometries, b) schematic representation of the descriptors (*d*, distance between the monomer core centers; and β dihedral angle formed by the monomer cores) used to account structural the degree of aggregation; and c) distribution of these parameters along the **D1** and **D2** MD trajectories.

The next point that we have to address is how the different aggregation properties of **1** and **2** modify their photophysics. With this aim, we calculated vertical excitation energies, at TD-DFT level, over a series of representative MD snapshots (see first part of the Methodological section). In a first stage, we have checked the suitability of our MD geometries to describe the main absorption features of **1** and **2** by comparing the averaged spectra obtained from the MD trajectories of the monomers (**M1** and **M2**) with the absorption spectrum obtained from Gaussian convolution (0.09 eV) of the vertical TD-DFT excitation energies and oscillator strengths on the DFT optimized GS geometry (see Figure S4). Interestingly, the overall shape of the QM spectra is well reproduced by the MD averaged ones. More importantly, despite showing some quantitative

deviations, both QM and MD averaged spectra show an identical behaviour concerning the nature of the three lowest excited states, with the bright S_1 state much lower in energy with respect to the dark S_2 and S_3 states (see Table S5 and Table S6), thus confirming that thermal effects play a minor role in the absorption features of these systems. Furthermore, vertical excited states obtained from DFT or force field (FF) optimized geometries display similar exciton delocalization for the three excited states of interest (see Table S2 and Figure S2), further validating the reliability of the FF procedure.

Now that we have verified that our MD protocol is robust enough to properly sample the conformation space of S_0 while properly describing the electronic characteristics of S_1, we can evaluate the impact of different aggregation motifs on the excited state properties. To this end, we have calculated on the snapshots extracted from the respective MD trajectories, two descriptors describing the excitonic properties of **D1** and **D2**: the participation ratio (PR), which provides an estimation of the number of monomers involved in the excitation; and the charge transfer (CT) coefficient describing the transfer of the electronic density from one monomer to the other. These two quantities calculated for the lowest-energy states (1.1-1.7 eV) are displayed in Figure 5.

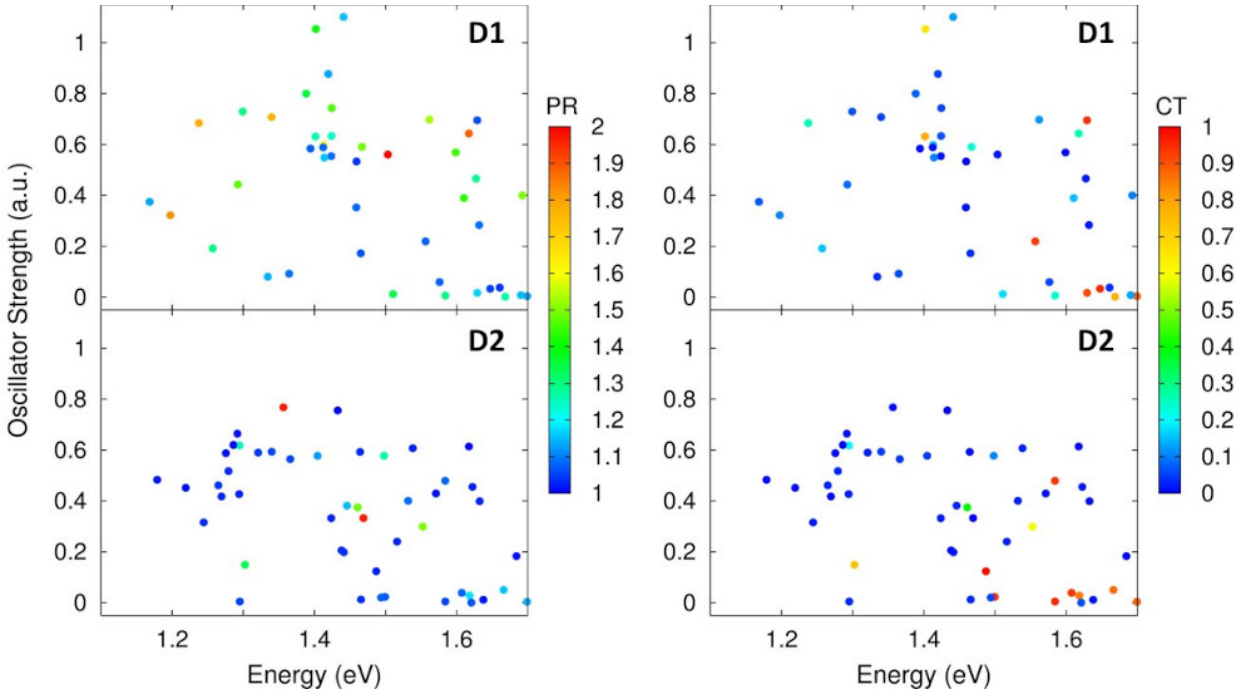

Figure 5. Colour maps representing the participation ratio (PR, left) and charge transfer (CT, right panel) values for the lowest energy states obtained from the **D1** (top) and **D2** (bottom) MD trajectories, as a function of their excitation energy (x-axis) and their oscillator strength (y-axis). The colour scales are depicted in the right part of each graph.

Clearly, the different structural arrangement, and in particular the strong aggregation present in **D1,** lead to a larger PR values (~1.4 for many states) with respect to **D2**, where almost all excitations where strictly localized over one single molecule (PR=1). Conversely, both **D1** and **D2** presented CT values very close to 1 for all states, hence excluding the presence of CT excitons even for **D1**, a result that further reinforces the argument against the population of CT state via intramolecular deformation. The same tendency is also reproduced for the higher excited states as shown in Figure S5. Another important question to address concerns the type of aggregates, namely H or J, since this is also related to the red- or blue-shift of the excitation energy. To do that, we calculated the orientational factor $\varkappa$, given by the relative positions of the transition dipole

moments of the two monomers and thus by the type of aggregation present in the dimers. Indeed, $\varkappa$ will be positive/negative for H-/J- aggregates, respectively (see Experimental section).[61] The distribution of the $\varkappa$ values, obtained from snapshots of the **D1** and **D2** trajectories are shown in Figure S6. Despite their different aggregation behavior, a comparable number of positive and negative $\varkappa$ values were obtained for both **D1** and **D2**. Interestingly, these results confirm that even the more compact **D1** presents a rather weak excitonic coupling presenting a coexistence of J- and H-aggregates and a rapid interconversion among them.

In turn, these finding imply that the different photophysical properties, and in particular the emissive or thermal deactivation, cannot be explained in terms of electronic factors and radiative recombination, only. This conclusion motivated us to evaluate the non-radiative deactivation pathways present in both solution and aggregated-state, by performing PCA of the MD trajectories. This type of analysis quantifies which are the most prominent motions by extracting the principal components of the covariance matrix of the atomic positions along the MD run. Therefore, the main eigenvalues and their corresponding eigenvectors obtained by PCA can be directly connected with those atomic motions, i.e. normal modes, which are dominating the global displacement. The representation of the most important PCA eigenvector and its corresponding eigenvalue for the four MD runs are displayed in Figure 6.

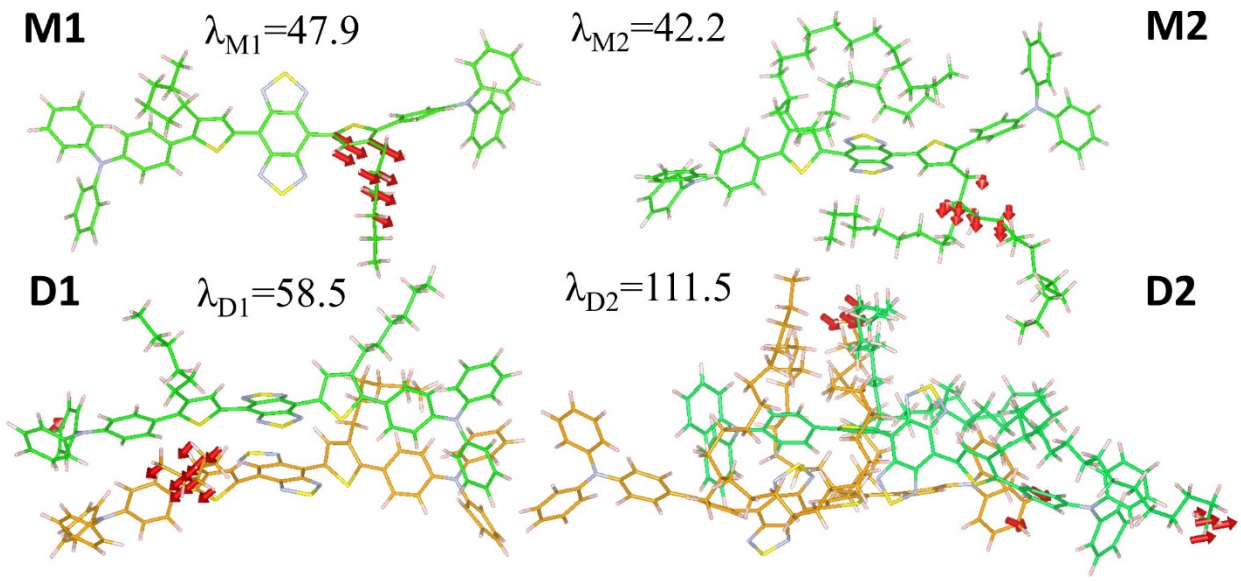

Figure 6. Vector representation of the main displacements as obtained from PCA with their correspondent eigenvalues in nm/s^{2}N, for the MD trajectories of **M1, M2**, **D1** and **D2**. For the shake of a better visualization, only the ten most important eigenvectors are represented here.

Due to their high flexibility, the largest PCA eigenvectors involve atomic motions of the alkyl chains for all MD runs. The same type of atomic displacements was also found for the three largest eigenvectors (see Figure S7). A further analysis of the standard deviation of the dihedral angles belonging to the alkyl chains confirmed that these large motions are originated by those dihedrals which are located in the center of the chain (see Table S7). Not surprisingly, both **1** and **2** display similar PCA eigenvalues in solution, what is consistent with the similar quantum yields achieved experimentally by both dyes in this type of environment. This finding clearly evidences that the intrinsic motion alkyl chains of the isolated dyes cannot be responsible of the emission line quenching. More strikingly, the PCA eigenvalues estimated in the aggregated-state for **1** and **2** were clearly diverging. The aggregation of **D1** monomer cores is somehow hampering the interaction between the side chains due to the close contact of the monomer cores (see Figure 4-

a), thus resulting in small PCA eigenvalues (being close to the ones observed in solution). Contrarily, the interaction between the bulky chains of **2** induces larger collective motions for these groups, which resulted in PCA eigenvalues two times larger with respect to **1**. As a matter of fact, we found the same trends in the PCA eigenvalues for **1** vs **2** dyes whether we considered atomic masses in the computation of these quantities or not (see Table S8). To sum up, we can infer that the contact between the alkyl chains of **2** in the aggregated-state activates large amplitude vibrational modes that are able to generate thermal deactivation of the excited state. This phenomenon seems to be at the origin of the light triggered heat dissipation showed by these dyes in the solid state, and it clearly points to the use of long bulky chains in the chemical design as the best strategy to enhance the photothermal properties of small organic molecules.

Conclusions

Herein we have carried out a combined TD-DFT/MD computational study of the relaxation mechanisms of planar D-π-A-π-D dyes, used as potential phototherapeutic agents, as a function of their peripheral groups and their environment (solution vs aggregation). In a first stage, we discerned the relaxation pathways followed by these dyes in solution upon NIR irradiation. Our calculations clearly revealed that only S_1 state is accessible in solution, internal conversion to other excited states was excluded since it would lead to unfavourable energetic pathways (more than 50 times kT). Afterwards, we evaluated the impact of the molecular packing on the excited state properties of the dyes with both short- and long- peripheral groups. Despite their distinct packing structures (compact and disordered for short- and long- chains, respectively), the absence of intermolecular CT and the similar type of H-/J- aggregation observed for both shielding groups, discarded a major effect of this factor on their different emission properties observed experimentally. Finally, the possible non-radiative deactivation processes were examined by

estimating the main eigenvectors obtained via PCA. This analysis demonstrated that while in solution both type of chains behaves similarly, in the aggregated-state the interaction of the longest peripheral chains triggers collective motions that can open thermal deactivation channels and that are absent in the shortest-chain analogous.

This work clearly evidenced that the origin of the excellent photothermal properties exhibited by this type of dyes are to be sought in the non-radiative relaxation induced by the aggregation-dependent activation of the intermolecular peripheral chain modes. With the results presented here we aim to encourage the PTT community to put more efforts in the design of NIR activated organic dyes where the interaction and motion of the shielding groups can be optimized and rationalized.

ASSOCIATED CONTENT

Supporting Information

The Supporting Information is available free of charge on the ACS Publications website. Tables and Figures related with the geometrical and excited state properties of the studied dyes in their static and dynamically relaxed structures.

AUTHOR INFORMATION

Corresponding Authors

Valentin Diez-Cabanes- *Université de Lorraine & CNRS, Laboratoire de Physique et Chimie Théoriques (LPCT), UMR 7019, F-54000, Nancy, France* ORCID: https://orcid.org/0000-0002-6234-2749. Email: valentin.diez-cabanes@univ-lorraine.fr

Mariachiara Pastore- *Université de Lorraine & CNRS, Laboratoire de Physique et Chimie Théoriques (LPCT), UMR 7019, F-54000, Nancy, France*. ORCID: https://orcid.org/0000-0003-4793-1964. Email: mariachiara.pastore@univ-lorraine.fr

Authors

Antonio Monari- *Université de Lorraine & CNRS, Laboratoire de Physique et Chimie Théoriques (LPCT), UMR 7019, F-54000, Nancy, France* ORCID: https://orcid.org/0000-0001-9464-1463

Notes

The authors declare no competing financial interest.

ACKNOWLEDGMENT

The authors gratefully acknowledge University of Lorraine, CNRS and the European Regional Development Funds under the Programme opérationnel FEDER-FSE Lorraine et Massif des Vosges 2014-2020 with the projects "Fire Light" ("Photo-bio-active molecules and nanoparticles") and COMETE (COnception in silico de Matériaux pour l'EnvironnemenT et l'Energie) for financial support. Computational resources were provided by the LPCT local cluster.

References

(1) Ban, Q.; Bai, T.; Duan, X.; Kong, J. Noninvasive Photothermal Cancer Therapy Nanoplatforms: Via Integrating Nanomaterials and Functional Polymers. *Biomater. Sci.* **2017**, *5* (2), 190–210. https://doi.org/10.1039/c6bm00600k.

(2) Chen, H.; Zhao, Y. Applications of Light-Responsive Systems for Cancer Theranostics. *ACS Appl. Mater. Interfaces* **2018**, *10* (25), 21021–21034.

https://doi.org/10.1021/acsami.8b01114.

(3) Liu, Y.; Bhattarai, P.; Dai, Z.; Chen, X. Photothermal Therapy and Photoacoustic Imaging: Via Nanotheranostics in Fighting Cancer. *Chem. Soc. Rev.* **2019**, *48* (7), 2053–2108. https://doi.org/10.1039/c8cs00618k.

(4) Li, X.; Lovell, J. F.; Yoon, J.; Chen, X. Clinical Development and Potential of Photothermal and Photodynamic Therapies for Cancer. *Nat. Rev. Clin. Oncol.* **2020**, *17* (11), 657–674. https://doi.org/10.1038/s41571-020-0410-2.

(5) Raju, G. S. R.; Dariya, B.; Mungamuri, S. K.; Chalikonda, G.; Kang, S. M.; Khan, I. N.; Sushma, P. S.; Nagaraju, G. P.; Pavitra, E.; Han, Y. K. Nanomaterials Multifunctional Behavior for Enlightened Cancer Therapeutics. *Semin. Cancer Biol.* **2021**, *69* (June), 178–189. https://doi.org/10.1016/j.semcancer.2019.08.013.

(6) Fernandes, N.; Rodrigues, C. F.; Moreira, A. F.; Correia, I. J. Overview of the Application of Inorganic Nanomaterials in Cancer Photothermal Therapy. *Biomater. Sci.* **2020**, *8* (11), 2990–3020. https://doi.org/10.1039/d0bm00222d.

(7) Khafaji, M.; Zamani, M.; Golizadeh, M.; Bavi, O. Inorganic Nanomaterials for Chemo/Photothermal Therapy: A Promising Horizon on Effective Cancer Treatment. *Biophys. Rev.* **2019**, *11* (3), 335–352. https://doi.org/10.1007/s12551-019-00532-3.

(8) Abadeer, N. S.; Murphy, C. J. Recent Progress in Cancer Thermal Therapy Using Gold Nanoparticles. *J. Phys. Chem. C* **2016**, *120* (9), 4691–4716. https://doi.org/10.1021/acs.jpcc.5b11232.

(9) Jung, H. S.; Verwilst, P.; Sharma, A.; Shin, J.; Sessler, J. L.; Kim, J. S. Organic Molecule-Based Photothermal Agents: An Expanding Photothermal Therapy Universe. *Chem. Soc. Rev.* **2018**, *47* (7), 2280–2297. https://doi.org/10.1039/c7cs00522a.

(10) Guo, B.; Huang, Z.; Shi, Q.; Middha, E.; Xu, S.; Li, L.; Wu, M.; Jiang, J.; Hu, Q.; Fu, Z.; Liu, B. Organic Small Molecule Based Photothermal Agents with Molecular Rotors for Malignant Breast Cancer Therapy. *Adv. Funct. Mater.* **2020**, *30* (5), 1–11. https://doi.org/10.1002/adfm.201907093.

(11) Dai, H.; Shen, Q.; Shao, J.; Wang, W.; Gao, F.; Dong, X. Small Molecular NIR-II Fluorophores for Cancer Phototheranostics. *Innov.* **2021**, *2* (1), 100082. https://doi.org/10.1016/j.xinn.2021.100082.

(12) Shi, Y.; Liu, M.; Deng, F.; Zeng, G.; Wan, Q.; Zhang, X.; Wei, Y. Recent Progress and Development on Polymeric Nanomaterials for Photothermal Therapy: A Brief Overview. *J. Mater. Chem. B* **2017**, *5* (2), 194–206. https://doi.org/10.1039/C6TB02249A.

(13) Pierini, F.; Nakielski, P.; Urbanek, O.; Pawlowska, S.; Lanzi, M.; De Sio, L.; Kowalewski, T. A. Polymer-Based Nanomaterials for Photothermal Therapy: From Light-Responsive to Multifunctional Nanoplatforms for Synergistically Combined Technologies. *Biomacromolecules* **2018**, *19* (11), 4147–4167. https://doi.org/10.1021/acs.biomac.8b01138.

(14) Yu, C.; Xu, L.; Zhang, Y.; Timashev, P. S.; Huang, Y.; Liang, X.-J. Polymer-Based Nanomaterials for Noninvasive Cancer Photothermal Therapy. *ACS Appl. Polym. Mater.* **2020**, *2* (10), 4289–4305. https://doi.org/10.1021/acsapm.0c00704.

(15) Liu, S.; Li, Y.; Kwok, R. T. K.; Lam, J. W. Y.; Tang, B. Z. Structural and Process Controls of AIEgens for NIR-II Theranostics. *Chem. Sci.* **2021**, *12* (10), 3427–3436. https://doi.org/10.1039/d0sc02911d.

(16) Shao, W.; Wei, Q.; Wang, S.; Li, F.; Wu, J.; Ren, J.; Cao, F.; Liao, H.; Gao, J.; Zhou, M.; Ling, D. Molecular Engineering of D-A-D Conjugated Small Molecule Nanoparticles for

High Performance NIR-II Photothermal Therapy. *Mater. Horizons* **2020**, *7* (5), 1379–1386. https://doi.org/10.1039/c9mh00660e.

(17) Guo, B.; Sheng, Z.; Hu, D.; Li, A.; Xu, S.; Manghnani, P. N.; Liu, C.; Guo, L.; Zheng, H.; Liu, B. Molecular Engineering of Conjugated Polymers for Biocompatible Organic Nanoparticles with Highly Efficient Photoacoustic and Photothermal Performance in Cancer Theranostics. *ACS Nano* **2017**, *11* (10), 10124–10134. https://doi.org/10.1021/acsnano.7b04685.

(18) Yang, Q.; Ma, H.; Liang, Y.; Dai, H. Rational Design of High Brightness NIR-II Organic Dyes with S-D-A-D-S Structure. *Accounts Mater. Res.* **2021**. https://doi.org/10.1021/accountsmr.0c00114.

(19) Nomura, S.; Morimoto, Y.; Tsujimoto, H.; Arake, M.; Harada, M.; Saitoh, D.; Hara, I.; Ozeki, E.; Satoh, A.; Takayama, E.; Hase, K.; Kishi, Y.; Ueno, H. Highly Reliable, Targeted Photothermal Cancer Therapy Combined with Thermal Dosimetry Using a near-Infrared Absorbent. *Sci. Rep.* **2020**, *10* (1), 1–7. https://doi.org/10.1038/s41598-020-66646-x.

(20) Yoon, H. J.; Lee, H. S.; Lim, J. Y.; Park, J. H. Liposomal Indocyanine Green for Enhanced Photothermal Therapy. *ACS Appl. Mater. Interfaces* **2017**, *9* (7), 5683–5691. https://doi.org/10.1021/acsami.6b16801.

(21) Sevieri, M.; Silva, F.; Bonizzi, A.; Sitia, L.; Truffi, M.; Mazzucchelli, S.; Corsi, F. Indocyanine Green Nanoparticles: Are They Compelling for Cancer Treatment? *Front. Chem.* **2020**, *8* (July), 1–9. https://doi.org/10.3389/fchem.2020.00535.

(22) Cai, Y.; Liang, P.; Tang, Q.; Yang, X.; Si, W.; Huang, W.; Zhang, Q.; Dong, X. Diketopyrrolopyrrole-Triphenylamine Organic Nanoparticles as Multifunctional Reagents for Photoacoustic Imaging-Guided Photodynamic/Photothermal Synergistic Tumor

Therapy. *ACS Nano* **2017**, *11* (1), 1054–1063. https://doi.org/10.1021/acsnano.6b07927.

(23) Zhao, Z.; Chen, C.; Wu, W.; Wang, F.; Du, L.; Zhang, X.; Xiong, Y.; He, X.; Cai, Y.; Kwok, R. T. K.; Lam, J. W. Y.; Gao, X.; Sun, P.; Phillips, D. L.; Ding, D.; Tang, B. Z. Highly Efficient Photothermal Nanoagent Achieved by Harvesting Energy via Excited-State Intramolecular Motion within Nanoparticles. *Nat. Commun.* **2019**, *10* (1), 1–11. https://doi.org/10.1038/s41467-019-08722-z.

(24) Qi, J.; Fang, Y.; Kwok, R. T. K.; Zhang, X.; Hu, X.; Lam, J. W. Y.; Ding, D.; Tang, B. Z. Highly Stable Organic Small Molecular Nanoparticles as an Advanced and Biocompatible Phototheranostic Agent of Tumor in Living Mice. *ACS Nano* **2017**, *11* (7), 7177–7188. https://doi.org/10.1021/acsnano.7b03062.

(25) Liu, S.; Zhou, X.; Zhang, H.; Ou, H.; Lam, J. W. Y.; Liu, Y.; Shi, L.; Ding, D.; Tang, B. Z. Molecular Motion in Aggregates: Manipulating TICT for Boosting Photothermal Theranostics. *J. Am. Chem. Soc.* **2019**, *141* (13), 5359–5368. https://doi.org/10.1021/jacs.8b13889.

(26) Wang, D.; Lee, M. M. S.; Xu, W.; Shan, G.; Zheng, X.; Kwok, R. T. K.; Lam, J. W. Y.; Hu, X.; Tang, B. Z. Boosting Non-Radiative Decay to Do Useful Work: Development of a Multi-Modality Theranostic System from an AIEgen. *Angew. Chemie - Int. Ed.* **2019**, *58* (17), 5628–5632. https://doi.org/10.1002/anie.201900366.

(27) Ni, J. S.; Zhang, X.; Yang, G.; Kang, T.; Lin, X.; Zha, M.; Li, Y.; Wang, L.; Li, K. A Photoinduced Nonadiabatic Decay-Guided Molecular Motor Triggers Effective Photothermal Conversion for Cancer Therapy. *Angew. Chemie - Int. Ed.* **2020**, *59* (28), 11298–11302. https://doi.org/10.1002/anie.202002516.

(28) D'Avino, G.; Muccioli, L.; Castet, F.; Poelking, C.; Andrienko, D.; Soos, Z. G.; Cornil, J.;

Beljonne, D. Electrostatic Phenomena in Organic Semiconductors: Fundamentals and Implications for Photovoltaics. *J. Phys. Condens. Matter* **2016**, *28* (43), 433002. https://doi.org/10.1088/0953-8984/28/43/433002.

(29) Mennucci, B. Polarizable Continuum Model. *Wiley Interdiscip. Rev. Comput. Mol. Sci.* **2012**, *2* (3), 386–404. https://doi.org/10.1002/wcms.1086.

(30) Ghosh, R.; Spano, F. C. Excitons and Polarons in Organic Materials. *Acc. Chem. Res.* **2020**, *53* (10), 2201–2211. https://doi.org/10.1021/acs.accounts.0c00349.

(31) Hestand, N. J.; Spano, F. C. Interference between Coulombic and CT-Mediated Couplings in Molecular Aggregates: H- to J-Aggregate Transformation in Perylene-Based π-Stacks. *J. Chem. Phys.* **2015**, *143* (24), 244707. https://doi.org/10.1063/1.4938012.

(32) Mei, J.; Leung, N. L. C.; Kwok, R. T. K.; Lam, J. W. Y.; Tang, B. Z. Aggregation-Induced Emission: Together We Shine, United We Soar! *Chem. Rev.* **2015**, *115* (21), 11718–11940. https://doi.org/10.1021/acs.chemrev.5b00263.

(33) Liu, S.; Li, Y.; Zhang, H.; Zhao, Z.; Lu, X.; Lam, J. W. Y.; Tang, B. Z. Molecular Motion in the Solid State. *ACS Mater. Lett.* **2019**, *1* (4), 425–431. https://doi.org/10.1021/acsmaterialslett.9b00292.

(34) Hong, Y.; Lam, J. W. Y.; Tang, B. Z. Aggregation-Induced Emission. *Chem. Soc. Rev.* **2011**, *40* (11), 5361–5388. https://doi.org/10.1039/c1cs15113d.

(35) Mei, J.; Hong, Y.; Lam, J. W. Y.; Qin, A.; Tang, Y.; Tang, B. Z. Aggregation-Induced Emission: The Whole Is More Brilliant than the Parts. *Adv. Mater.* **2014**, *26* (31), 5429–5479. https://doi.org/10.1002/adma.201401356.

(36) Huang, Y.; Xing, J.; Gong, Q.; Chen, L. C.; Liu, G.; Yao, C.; Wang, Z.; Zhang, H. L.; Chen, Z.; Zhang, Q. Reducing Aggregation Caused Quenching Effect through Co-Assembly of

PAH Chromophores and Molecular Barriers. *Nat. Commun.* **2019**, *10* (1), 1–9. https://doi.org/10.1038/s41467-018-08092-y.

(37) Liu, S.; Chen, C.; Li, Y.; Zhang, H.; Liu, J.; Wang, R.; Wong, S. T. H.; Lam, J. W. Y.; Ding, D.; Tang, B. Z. Constitutional Isomerization Enables Bright NIR-II AIEgen for Brain-Inflammation Imaging. *Adv. Funct. Mater.* **2020**, *30* (7), 1–10. https://doi.org/10.1002/adfm.201908125.

(38) Li, Y.; Cai, Z.; Liu, S.; Zhang, H.; Wong, S. T. H.; Lam, J. W. Y.; Kwok, R. T. K.; Qian, J.; Tang, B. Z. Design of AIEgens for Near-Infrared IIb Imaging through Structural Modulation at Molecular and Morphological Levels. *Nat. Commun.* **2020**, *11* (1), 1–10. https://doi.org/10.1038/s41467-020-15095-1.

(39) Adamo, C.; Jacquemin, D. The Calculations of Excited-State Properties with Time-Dependent Density Functional Theory. *Chem. Soc. Rev.* **2013**, *42* (3), 845–856. https://doi.org/10.1039/c2cs35394f.

(40) Laurent, A. D.; Adamo, C.; Jacquemin, D. Dye Chemistry with Time-Dependent Density Functional Theory. *Phys. Chem. Chem. Phys.* **2014**, *16* (28), 14334–14356. https://doi.org/10.1039/c3cp55336a.

(41) Segalina, A.; Assfeld, X.; Monari, A.; Pastore, M. Computational Modeling of Exciton Localization in Self-Assembled Perylene Helices: Effects of Thermal Motion and Aggregate Size. *J. Phys. Chem. C* **2019**, *123* (11), 6427–6437. https://doi.org/10.1021/acs.jpcc.9b00494.

(42) Olivier, Y.; Sancho-Garcia, J. C.; Muccioli, L.; D'Avino, G.; Beljonne, D. Computational Design of Thermally Activated Delayed Fluorescence Materials: The Challenges Ahead. *J. Phys. Chem. Lett.* **2018**, *9* (20), 6149–6163. https://doi.org/10.1021/acs.jpclett.8b02327.

(43) Peng, Q.; Shuai, Z. Molecular Mechanism of Aggregation-induced Emission. *Aggregate* **2021**, *e91* (February), 1–20. https://doi.org/10.1002/agt2.91.

(44) Yanai, T.; Tew, D. P.; Handy, N. C. A New Hybrid Exchange-Correlation Functional Using the Coulomb-Attenuating Method (CAM-B3LYP). *Chem. Phys. Lett.* **2004**, *393* (1–3), 51–57. https://doi.org/10.1016/j.cplett.2004.06.011.

(45) Wiggins, P.; Williams, J. A. G.; Tozer, D. J. Excited State Surfaces in Density Functional Theory: A New Twist on an Old Problem. *J. Chem. Phys.* **2009**, *131* (9). https://doi.org/10.1063/1.3222641.

(46) Plötner, J.; Tozer, D. J.; Dreuw, A. Dependence of Excited State Potential Energy Surfaces on the Spatial Overlap of the Kohn-Sham Orbitals and the Amount of Nonlocal Hartree-Fock Exchange in Time-Dependent Density Functional Theory. *J. Chem. Theory Comput.* **2010**, *6* (8), 2315–2324. https://doi.org/10.1021/ct1001973.

(47) Guido, C. A.; Mennucci, B.; Jacquemin, D.; Adamo, C. Planar vs. Twisted Intramolecular Charge Transfer Mechanism in Nile Red: New Hints from Theory. *Phys. Chem. Chem. Phys.* **2010**, *12* (28), 8016–8023. https://doi.org/10.1039/b927489h.

(48) Tomasi, J.; Mennucci, B.; Cammi, R. Quantum Mechanical Continuum Solvation Models. *Chem. Rev.* **2005**, *105* (8), 2999–3093. https://doi.org/10.1021/cr9904009.

(49) Plasser, F. TheoDORE: A Toolbox for a Detailed and Automated Analysis of Electronic Excited State Computations. *J. Chem. Phys.* **2020**, *152* (8), 084108. https://doi.org/10.1063/1.5143076.

(50) Martin, R. L. Natural Transition Orbitals. *J. Chem. Phys.* **2003**, *118* (11), 4775–4777. https://doi.org/10.1063/1.1558471.

(51) Frisch, M. J.; Trucks, G. W.; Schlegel, H. B.; Scuseria, G. E.; Robb, M. A.; Cheeseman, J.

R.; Scalmani, G.; Barone, V.; Petersson, G. a.; Nakatsuji, H.; Li, X.; Caricato, M.; Marenich, a. V.; Bloino, J.; Janesko, B. G.; Gomperts, R.; Mennucci, B.; Hratchian, H. P.; Ortiz, J. V.; Izmaylov, a. F.; Sonnenberg, J. L.; Williams; Ding, F.; Lipparini, F.; Egidi, F.; Goings, J.; Peng, B.; Petrone, A.; Henderson, T.; Ranasinghe, D.; Zakrzewski, V. G.; Gao, J.; Rega, N.; Zheng, G.; Liang, W.; Hada, M.; Ehara, M.; Toyota, K.; Fukuda, R.; Hasegawa, J.; Ishida, M.; Nakajima, T.; Honda, Y.; Kitao, O.; Nakai, H.; Vreven, T.; Throssell, K.; Montgomery Jr., J. a.; Peralta, J. E.; Ogliaro, F.; Bearpark, M. J.; Heyd, J. J.; Brothers, E. N.; Kudin, K. N.; Staroverov, V. N.; Keith, T. a.; Kobayashi, R.; Normand, J.; Raghavachari, K.; Rendell, a. P.; Burant, J. C.; Iyengar, S. S.; Tomasi, J.; Cossi, M.; Millam, J. M.; Klene, M.; Adamo, C.; Cammi, R.; Ochterski, J. W.; Martin, R. L.; Morokuma, K.; Farkas, O.; Foresman, J. B.; Fox, D. J. Gaussian 16, Revision C.01. 2016, p Gaussian, Inc., Wallingford CT.

(52) Diez-Cabanes, V.; Prampolini, G.; Francés-Monerris, A.; Monari, A.; Pastore, M. Iron's Wake: The Performance of Quantum Mechanical-Derived Versus General-Purpose Force Fields Tested on a Luminescent Iron Complex. *Molecules* **2020**, *25* (13), 1–21. https://doi.org/10.3390/molecules25133084.

(53) Wang, J.; Wolf, R. M.; Caldwell, J. W.; Kollman, P. A.; Case, D. A. Development and Testing of a General Amber Force Field. *J. Comput. Chem.* **2004**, *56531* (9), 1157–1174. https://doi.org/10.1002/jcc.20035.

(54) Wang, J.; Wang, W.; Kollman, P. A.; Case, D. A. Automatic Atom Type and Bond Type Perception in Molecular Mechanical Calculations. *J. Mol. Graph. Model.* **2006**, *25* (2), 247–260. https://doi.org/10.1016/j.jmgm.2005.12.005.

(55) Sousa, A. W.; Vranken, W. F. Open Access ACPYPE - AnteChamber PYthon Parser

InterfacE. *BMC Res. Notes* **2012**, *5*, 367.

(56) Pronk, S.; Páll, S.; Schulz, R.; Larsson, P.; Bjelkmar, P.; Apostolov, R.; Shirts, M. R.; Smith, J. C.; Kasson, P. M.; Van Der Spoel, D.; Hess, B.; Lindahl, E. GROMACS 4.5: A High-Throughput and Highly Parallel Open Source Molecular Simulation Toolkit. *Bioinformatics* **2013**, *29* (7), 845–854. https://doi.org/10.1093/bioinformatics/btt055.

(57) L. Martinez; Andrade, R.; Birgin, E. G.; Martinez, J. M. Packmol: A Package for Building Initial Configurations for Molecular Dynamics Simulations. *J. Comput. Chem.* **2009**, *30*, 2157–2164. https://doi.org/10.1002/jcc.21224.

(58) Bussi, G.; Donadio, D.; Parrinello, M. Canonical Sampling through Velocity Rescaling. *J. Chem. Phys.* **2007**, *126* (1), 014101. https://doi.org/10.1063/1.2408420.

(59) Parrinello, M.; Rahman, A. Polymorphic Transitions in Single Crystals: A New Molecular Dynamics Method. *J. Appl. Phys.* **1981**, *52* (12), 7182–7190. https://doi.org/10.1063/1.328693.

(60) van de Craats, A. M.; Stutzmann, N.; Bunk, O.; Nielsen, M. M.; Watson, M.; Müllen, K.; Chanzy, H. D.; Sirringhaus, H.; Friend, R. H. Meso-Epitaxial Solution-Growth of Self-Organizing Discotic Liquid-Crystalline Semiconductors. *Adv. Mater.* **2003**, No. 6, 495–499. https://doi.org/doi.org/10.1002/adma.200390114.

(61) Hestand, N. J.; Spano, F. C. Expanded Theory of H- and J-Molecular Aggregates: The Effects of Vibronic Coupling and Intermolecular Charge Transfer. *Chem. Rev.* **2018**, *118* (15), 7069–7163. https://doi.org/10.1021/acs.chemrev.7b00581.

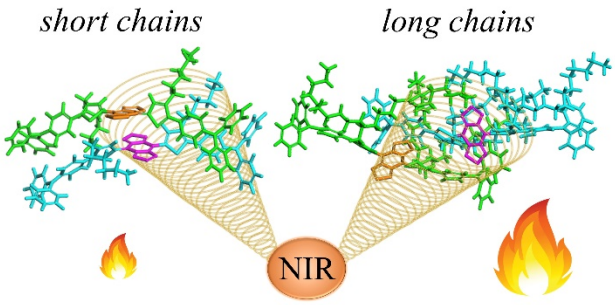

TOC Graphic